

Three-component modelling of O-rich AGB star winds

I. Effects of drift using forsterite

C. Sandin¹, L. Mattsson², K. L. Chubb³, M. Ergon^{4,1}, and P. M. Weillbacher⁵

¹ Department of Astronomy, AlbaNova University Center, Stockholm University, SE-10691 Stockholm, Sweden
e-mail: christer.sandin@astro.su.se

² Nordita, KTH Royal Institute of Technology and Stockholm University, Hannes Alfvéns väg 12, SE-10691 Stockholm, Sweden

³ Centre for Exoplanet Science, University of St Andrews, North Haugh, St Andrews, KY16 9SS, United Kingdom

⁴ The Oskar Klein Centre, AlbaNova, SE-10691 Stockholm, Sweden

⁵ Leibniz-Institut für Astrophysik Potsdam (AIP), An der Sternwarte 16, 14482 Potsdam, Germany

Submitted January 3, 2023; revised version submitted

ABSTRACT

Stellar winds of cool and pulsating asymptotic giant branch (AGB) stars enrich the interstellar medium with large amounts of processed elements and various types of dust. We present a first study on the influence of gas-to-dust drift on ab initio simulations of stellar winds of M-type stars driven by radiation pressure on forsterite particles. Our study is based on our radiation hydrodynamic model code T-800 that includes frequency-dependent radiative transfer, dust extinction based on Mie scattering, grain growth and ablation, gas-to-dust drift using one mean grain size, a piston that simulates stellar pulsations, and an accurate high spatial resolution numerical scheme. To enable this study, we calculated new gas opacities based on the ExoMol database, and we extended the model code to handle the formation of minerals that may form in M-type stars. We discern effects of drift by comparing drift models to our new and extant non-drift models. Three out of four new drift models show high drift velocities, 87–310 km s⁻¹. Our new drift model mass-loss rates are 1.7–13 per cent of the corresponding values of our non-drift models, but compared to results of two extant non-drift models that use the same stellar parameters, these same values are 0.33–1.5 per cent. Meanwhile, a comparison of other properties such as the expansion velocity and grain size show similar values. Our results, which are based on single-component forsterite particles, show that the inclusion of gas-to-drift is of fundamental importance in stellar wind models driven by such transparent grains. Assuming that the drift velocity is insignificant, properties such as the mass-loss rate may be off from more realistic values by a factor fifty and more.

Key words. hydrodynamics – radiative transfer – stars: atmospheres – stars: AGB and post-AGB – stars: mass-loss – stars: winds, outflows

1. Introduction

Stellar winds rule the final and decisive stages of evolution of low-to-intermediate mass stars when they ascend the asymptotic giant branch (AGB). The dynamic AGB stage involves increasing luminosities, low effective temperatures, and stellar pulsations. Dust formation begins at a couple of stellar radii where temperatures are low enough to prevent the newly formed grains from evaporating, and new dust grains absorb or scatter the radiation and in that way attain a momentum. The grains accelerate outwards and collide with particles in the gas that are dragged along as the particles drift through the same gas. Considering all the needed physics, it is a physical problem of a kind to simulate the resulting dust-driven wind where low expansion velocities are about 10 km s⁻¹ and high mass-loss rates vary from 10⁻⁸ up to, in extreme cases, 10⁻⁴ M_⊙ yr⁻¹.

Depending on what element dominates, AGB stars are either oxygen-rich (M-type stars) or carbon-rich (C-type stars). The dichotomy is reflected in stellar wind models where dust formation in a carbon-rich chemistry is more simple where mostly amor-

phous carbon forms. Other types of dust and minerals do not appear to form in sufficient numbers to be influential.

Dust formation in an oxygen-rich chemistry is more complex. Spectra of circumstellar envelopes of M-type AGB stars show characteristic silicate features at 9.7 and 18 μm (see, e.g. Woolf & Ney 1969; Low 1970; Molster et al. 2002; Dorschner 2010; Molster et al. 2010). These features indicate that silicon-containing grains are a dominant component in M-type AGB stars. Crystalline silicate dust with features at 11, 23, 28, 33, and 69 μm is also seen (Blommaert et al. 2014), but the crystallinity does not appear to be correlated with mass-loss rates (Liu et al. 2017). Various minerals form depending on the availability of elements that are part of the different minerals, including olivine, pyroxene, and iron (Gail & Sedlmayr 1999).

Metallic iron, moreover, appears to be a significant component in the cosmic dust budget owing to the large iron depletion seen in the interstellar medium (Mattsson et al. 2019). Such grains can probably form in AGB atmospheres and their scattering cross-sections are typically large, so if they form in sufficient number, they may contribute to the driving of the wind. Gail &

Sedlmayr (2014, hereafter, GS14) present a refined and in many ways complete [rates-based] approach on how to implement mineral formation in both carbon and oxygen-rich chemistries.

Höfner (2008, hereafter H08) presents first working models (DARWIN) of stellar winds in oxygen-rich chemistry. She finds that the dust scattering cross section of larger micron-sized iron-free silicate particles provide a high enough radiative pressure to drive a stellar wind. Bladh & Höfner (2012) and Bladh et al. (2013) then argue, based mostly on parameterized models of dust, that forsterite and enstatite are the most likely dust species that drive the stellar wind; they also present photometric properties of models that agree well with observations. Bladh et al. (2015) present a larger set of radiation hydrodynamic models that include non-equilibrium dust formation. The authors conclude that they can calculate mass-loss rates as well as spectra, which visual and near-IR diagnostics agree with observations. Bladh et al. (2019, hereafter B19) present the most extensive set of calculated M-type stellar wind models available this far. Whilst the stellar wind models of H08 up to B19 show agreement with observations, they are based on some assumptions that we find interesting to explore in more detail. The authors emphasize that they calculate high mass-loss rates and photometric properties that agree well with observations. They also point out that there are few free parameters in their radiation hydrodynamic models. In particular, the only such free parameter they mention is the seed particle abundance. The authors, moreover, appear to use sticking coefficients that are always set to unity (1) to form as much dust as possible, instead of using extant lower empirically based values. Additional assumptions include only modelling one (or two) dust species at a time.

Physical arguments imply that effects of drift are stronger in these winds than in carbon-rich environments (Mattsson & Sandin 2021, hereafter MS21). Only one extant study addresses effects of drift, whilst assuming very low drift velocities, lacking any "evidence" for higher values (Tosi et al. 2022). We think there is good reason to check the influence of drift on results more carefully. As we show here, drift velocities turn out to be dramatically higher in models of M-type stars than in models of C-type stars. Correspondingly, we also find dramatically lower mass-loss rates. We are – with our physically and numerically extended models – unable to reproduce the higher valued mass-loss rates of DARWIN that the authors base their results of good agreement with observations on. Whilst more reliable observations of mass loss show higher mass-loss rates, it is clear that something important is missing in the picture of understanding the formation of stellar winds in M-type stars.

Extant ab initio stellar wind models that include drift are all based on a carbon-rich chemistry. Sandin & Mattsson (2020, hereafter Paper V) include frequency-dependent radiative transfer and opacity tables of both the gas and the dust, and calculate models at high spatial resolution: results indicate important differences between drift models and position-coupled (PC, i.e. non-drift) models. Mass-loss rates, expansion velocities, and yields of dust are affected. An additional example of a carbon-rich model where drift is found to be an important component to understand the observations is presented in a study of grain alignment about IRC+10°216 (Andersson et al. 2022); this object shows a very high mass-loss rate (of $2\text{--}8 \times 10^{-5} M_{\odot} \text{yr}^{-1}$), where our model nevertheless show a drift velocity that is twice as high as the expansion velocity.

We use our simulation code T-800 of Paper V and extend it with the rates-based description of dust formation in an oxygen-rich chemistry. Specifically, we here focus on a wind where only forsterite is formed. To enable this study, we calculated new

gas opacity tables for solar metallicities based on the ExoMol database (Tennyson et al. 2020), and also added free-free and bound-free opacities calculated using the JEKYLL code (Ergon et al. 2018; Ergon & Fransson 2022). We are thereby, for the first time, able to study time-dependent models using high spatial resolution in simulations that use an oxygen-rich chemistry that includes drift.

We first make semi-analytical predictions of the drift velocity in Sect. 2 to see what we can deduce based on simple physical arguments. Thereafter, we describe the physics features of our physically enhanced models in Sect. 3. Presentations of the modelling procedure and results follow in Sect. 4. We discuss the influence of drift on our results in Sect. 5 and close the paper with our conclusions in Sect. 6.

2. Semi-analytic predictions of drift

Before we engage in numerical and physical details of our updated version of T-800, we look at a simplified treatment of the oxygen-rich stellar-wind formation problem to estimate how high associated drift velocities could be. We address the balancing forces that give rise to the wind in Sect. 2.1. Thereafter we, anew, look at the concept of complete momentum coupling in Sect. 2.2 and conclude this analysis in Sect. 2.3.

2.1. Balancing dust extinction and radiation pressure

To estimate the drift velocity for a given set of stellar parameters, we need to estimate the radiation pressure on the dust component. Thus, we need to know the photon-to-dust grain momentum transfer efficiency. Absorption and scattering of photons by dust grains is modelled with the effective cross sections $\sigma_{\text{abs},\nu}$ and $\sigma_{\text{sca},\nu}$, where ν is the frequency. The efficiency of absorption and scattering, or the combination of the two (extinction), is usually defined relative to the geometric cross section σ . For spherical grains, $\sigma = \pi a^2$, where a is the grain radius. The absorption efficiency $Q_{\text{abs},\nu} = \sigma_{\text{abs},\nu}/\sigma$ is related to the extinction and scattering efficiencies $Q_{\text{ext},\nu} = \sigma_{\text{ext},\nu}/\sigma$ and $Q_{\text{sca},\nu} = \sigma_{\text{sca},\nu}/\sigma$, as

$$Q_{\text{abs},\nu} = Q_{\text{ext},\nu} - Q_{\text{sca},\nu}. \quad (1)$$

To calculate a correct radiation pressure, it is necessary to use the absorption efficiency (we name this term $Q_{\text{abs},\nu}(\text{pr})$ in Paper V),

$$Q_{\text{rp},\nu} = Q_{\text{ext},\nu} - g_{\text{sca},\nu} Q_{\text{sca},\nu} = Q_{\text{abs},\nu} - (g_{\text{sca},\nu} - 1) Q_{\text{sca},\nu}, \quad (2)$$

where $g_{\text{sca},\nu} = \langle \cos \theta \rangle_{\nu}$ is the average scattering angle. Mie theory (Bohren & Huffman 1983) provides these efficiencies as well as the average scattering angle.

In many extant works on AGB winds (e.g., Sandin & Höfner 2003; Mattsson et al. 2008, 2010), the radiation pressure is calculated assuming dust grains are small compared to the wavelength of the incident radiation. This, so called, small-particle limit (SPL) approximation leads to the simplification $Q_{\text{ext},\nu} = Q'_{\nu}/a$, where Q'_{ν} is a function of only the frequency (Wickramasinghe 1972). Figure 1 shows how $Q_{\text{rp},\nu}$, as computed based on Mie theory, compares to the corresponding SPL value of $Q_{\text{ext},\nu}$, using optical constants of Jäger et al. (2003). An important feature is the [blue] “peacock feather”-like region where the Mie-theory based radiation force on grains of radius a in an optically thin atmosphere is (where the Eddington flux $H_{\nu}(r) \approx 0.25(R_{\star}/r)^2$),

$$f_{\text{rad,d}} = \frac{\pi}{c} \left(\frac{R_{\star}}{r} \right)^2 n_{\text{d}}(a) \int_0^{\infty} a^2 Q_{\text{rp},\nu}(a) B_{\nu}(T_{\text{eff}}) d\nu, \quad (3)$$

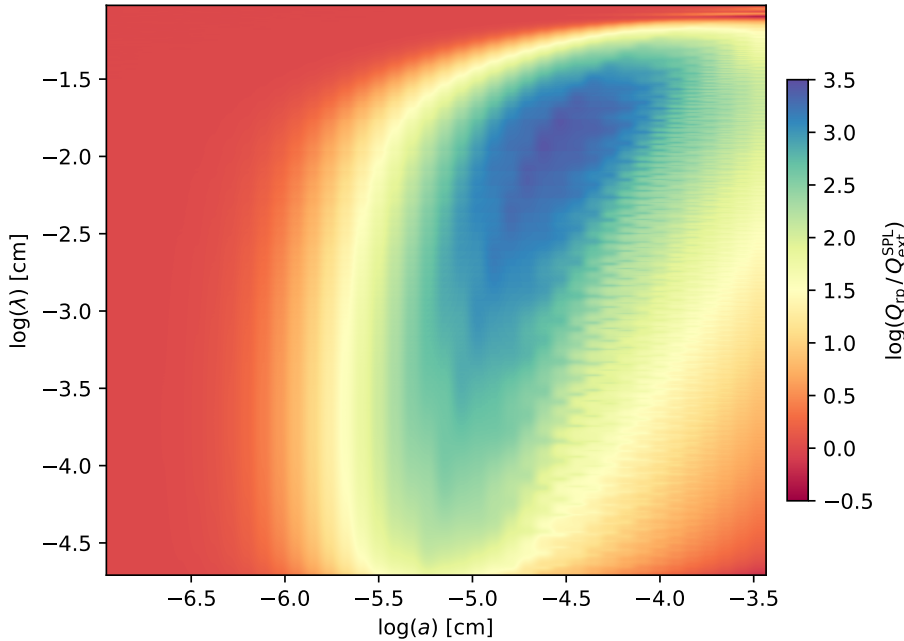


Fig. 1. Ratio of the radiation pressure efficiency $Q_{\text{rp},\nu}$ to the SPL extinction efficiency versus the grain radius and wavelength, assuming spherical forsterite grains.

where R_\star is the stellar radius, n_d the grain number density, and B_ν the Planck function. Grain sizes in the region of relevant values ($0.1 \lesssim a \lesssim 0.5 \mu\text{m}$) result in a radiation pressure about 300–30 times lower in the spectral region near the typical flux peak of M-type AGB stars ($\lambda \approx 1 \mu\text{m}$) than when the SPL is assumed.

2.2. Momentum coupling and equilibrium drift

In Paper V, complete momentum coupling (CMC) is defined as the case of force balance between radiation on the one hand and drag and gravity on the other hand, although the amount of momentum lost owing to the gravitational potential is negligible. Equating the radiation and drag forces is also a common definition of CMC.

Drift is a non-linear dynamic phenomenon, but simulations (in particular those of Paper V) show that an equilibrium tends to develop in most cases. Equilibrium drift can be defined as the situation where the Lagrangian derivatives of gas and dust velocity are equal, i.e., $dv/dt = du/dt$. This, in turn, means that the equilibrium drift velocity \dot{v}_D is constant with respect to time and that \dot{v}_D is governed by a simple algebraic equation instead of a hard-to-solve partial differential equation.

Assuming equilibrium drift and CMC defined as above, the drag force is $f_{\text{drag}} = f_{\text{rad},d} - f_{\text{grav},d}$. Defining the dimensionless variable

$$S_D = \frac{\dot{v}_D}{v_\zeta}, \quad \text{and} \quad v_\zeta = \sqrt{\zeta T_g} = \sqrt{\frac{128k_B}{9\pi\mu m_H} T_g},$$

where v_ζ is a modified thermal velocity, k_B is the Boltzmann constant, μ the mean molecular weight, m_H the mass of a hydrogen atom, and T_g the gas temperature. We then have

$$S_D^2 = -\frac{1}{2} + \left\{ \frac{1}{4} + \left(\frac{f_{\text{rad},d} - f_{\text{grav},d}}{f_\zeta} \right)^2 \right\}^{\frac{1}{2}}. \quad (4)$$

where $f_{\text{grav},d} \approx \rho_d GM_\star r^{-2}$ is the point-mass approximation for the gravitational force, ρ_d the dust density, G the Gravitational constant, and $f_\zeta = \pi a^2 n_d \rho_g v_\zeta^2$ can be seen as a thermal coupling

force between gas and dust; and here, ρ_g is the gas density. For a given mass-loss rate \dot{M} , wind expansion velocity u_∞ , luminosity L_\star , effective temperature T_{eff} , and stellar mass M_\star , we can now estimate the equilibrium drift velocity \dot{v}_D using the above equation in combination with the condition for mass conservation $\dot{M} = 4\pi r^2 \rho_g u_\infty$ and $L_\star = 4\pi \sigma_{\text{SB}} R_\star^2 T_{\text{eff}}^4$, where σ_{SB} is the Stefan-Boltzmann constant.

2.2.1. Predicted drift velocities

In Fig. 2, we show the expected equilibrium drift velocity \dot{v}_D versus grain radius a for the M_\star , $\log(L_\star)$, T_{eff} , and mass-loss rates of our detailed simulations (presented in Sect. 4.3). The stellar parameters were chosen to represent recent stellar evolution models (in particular those of Marini et al. 2023), but also observations (see, e.g., Uttenthaler et al. 2019, and references therein). The predictions from equilibrium theory are in acceptable agreement with our detailed modelling, overpredicting v_D by just a little more than a factor of two. Thus, we conclude there is a solid case for high drift velocities and that the maximum drift velocity of each curve occurs for grain radii that are quite typical for M-type AGB stars according to extant models (B19).

It is clear that a wind driven by radiation pressure on forsterite grains leads to high drift velocities, even in case of massive outflows. It has been argued that drift is negligible in winds associated with very high mass-loss rates (Höfner & Olofsson 2018), which seems to be the case for carbon stars (see Fig. 3a in Paper V); however, our more recent model of the stellar wind in IRC+10°216 says otherwise (see Sect. 4.3 and Fig. 8 in Andersson et al. 2022). But given that M-type AGB stars have wind speeds of $u_\infty \sim 10 \text{ km s}^{-1}$ (as is revealed by radio observations of Olofsson et al. 2002; González Delgado et al. 2003) and typical grain sizes $a \approx 0.5 \mu\text{m}$, the drift factor $\tilde{\mathcal{F}}_D^\infty = 1 + v_D/u_\infty > 2$ also for intense outflows. A drift factor $\tilde{\mathcal{F}}_D^\infty > 2$ corresponds to a situation where the drift velocity v_D exceeds the gas expansion velocity u_∞ and the dust mass-loss rate increases by as much when compared to the gas mass loss rate, see Eq. (32) in Paper V. We tentatively conclude that including

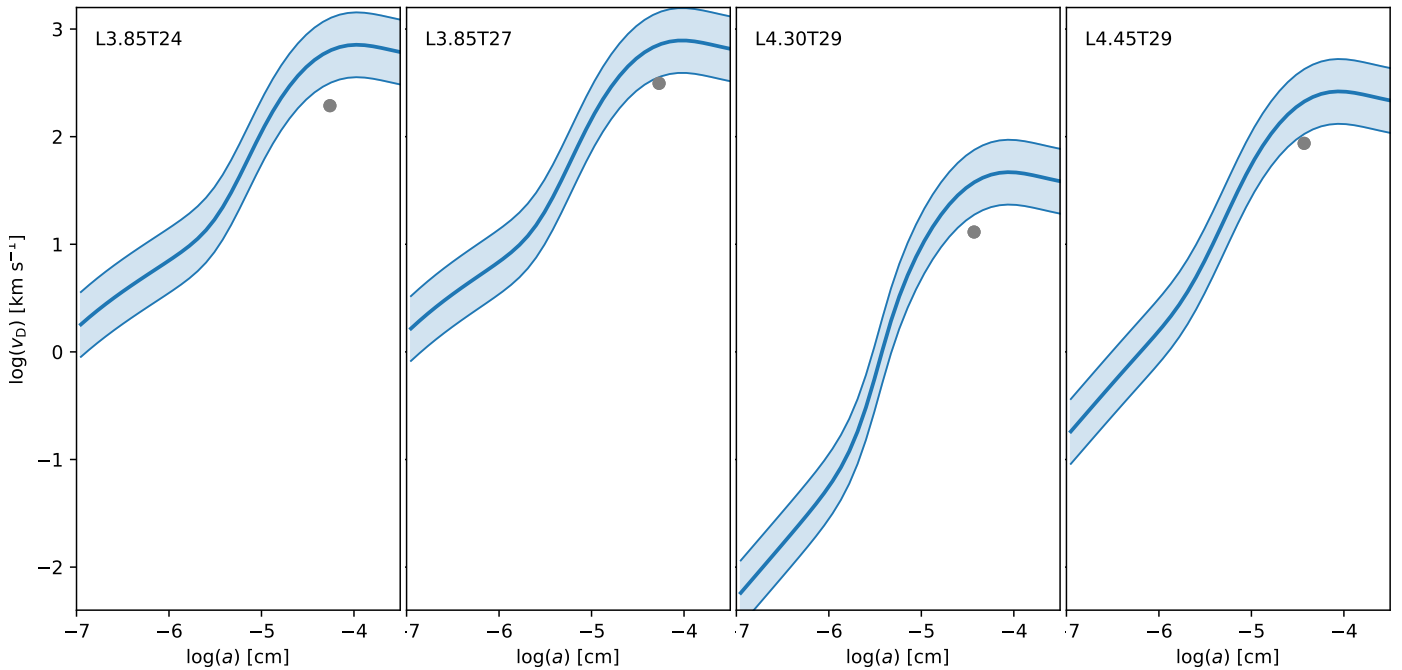


Fig. 2. Equilibrium drift velocity \hat{v}_D versus grain radius, assuming CMC. Four panels show different parameter configurations considered in the present study; all panels use the same ordinate range. The shaded regions show factor-of-two variations of the semi-analytical results based on equilibrium theory (shown by solid lines). The bullets indicate the locations of the two numerical simulations with drift presented in Sect. 4.3.

drift in the modelling of M-type AGB stars is of absolute fundamental importance, as PC models do not provide a correct result even in the high-mass-loss limit. As we shall see, this conclusion is confirmed by our detailed modelling, described below.

2.3. Physical interpretation of the PC assumption

The PC assumption is incompatible with the idea that AGB winds form by friction between radiatively accelerated dust grains and gas particles. MS21 argue that there is no realistic physical limiting case which leads to PC. Whilst this must still be true, we shall here discuss the (unrealistic) limit where PC is formally true.

Considering Eq. (4), we note that $(f_{\text{rad,d}} - f_{\text{grav,d}})/f_{\zeta} \ll 1$ implies $S_D = 0$, i.e., no drift. If we ignore the case $f_{\text{rad,d}} = f_{\text{grav,d}}$, this limit requires that f_{ζ} is very large and, in particular, much larger than the net radiation force $\tilde{f}_{\text{rad,d}} = f_{\text{rad,d}} - f_{\text{grav,d}}$. For this to occur in the case given in the previous section (with $f_{\text{rad,d}}$ obtained from Eq. (3)), the modified thermal velocity v_{ζ} has to be of the order 100 km s^{-1} unless ρ_g is several orders of magnitude higher than expected in a realistic wind. Such a high v_{ζ} corresponds to gas temperatures of the order 10^5 K , which is entirely unrealistic. It is fair to say that the physical interpretation (or consequence) of the assumption of PC is absurd. The semi-analytic predictions of drift velocity presented here provide a solid theoretically founded reason for pursuing detailed modelling of winds of M-type AGB stars with gas and dust treated as dynamically decoupled phases.

3. Model features and improvements of T-800

The model features of our radiation hydrodynamic model code T-800 is described in Paper V. As in the case of a C-rich chemistry, we model three components in the O-rich chemistry de-

scribed here: the gas, the radiation field, and a dust component consisting of forsterite (Fo) mineral grains.

In comparison to the moments method used to describe dust formation in the C-rich chemistry, we replace the four dust moment equations (K_0 – K_3) with one rate equation for the formation of each mineral k , and the carbon number density equation (Eq. (5) in Paper V) with corresponding equations for each affected tracer element j . All physics of mineral formation in oxygen-rich chemistry we require is developed and described by Gail & Sedlmayr (1999) and GS14. The adjusted equations are

$$\frac{\partial}{\partial t} n_{d,k} N_k + \nabla \cdot (n_{d,k} N_k v_k) = q_k, \quad (5)$$

$$\frac{\partial}{\partial t} n_j + \nabla \cdot (n_j u) = -v_k^j q_k, \quad (6)$$

where t is the time, $n_{d,k}$ the seed particle density, N_k the number of monomers, v_k the mean dust particle velocity, q_k the sum of the source and sink terms owing to grain formation, n_j the tracer element atom number density, v_k^j the number of tracer element atoms per monomer, and u the gas velocity. In this approach, there is no description of nucleation. Instead, seed particles of each individual species are assumed to exist everywhere and

$$n_{d,k} = \rho_g \frac{\epsilon_k}{m_u \mu}, \quad (7)$$

where ϵ_k the seed particle abundance, m_u the atomic mass constant, and $\mu = 1.26$.

3.1. The mineral rate equation

The rate equations track the number of monomers N_k throughout the model domain. The rate equation source term owing to grain growth, evaporation, and destruction is

$$q_k = n_{d,k} \left[4\pi a_k^2 (J_{\text{gr},k} - J_{\text{ev},k}) - \frac{1}{\tau_{\text{sp},n}^k} \right], \quad (8)$$

where a_k is the particle radius, J_{gr} (J_{ev}) the growth (evaporation) rate, and $1/\tau_{\text{sp},n}$ the rate of non-thermal sputtering. The grain radius is described using the grain volume V_k and the monomer volume V_1 ,

$$a_k = \left(\frac{3V_k}{4\pi} \right)^{\frac{1}{3}}, \quad V_k = N_k V_{1,k}, \quad V_{1,k} = \frac{\mathcal{A}_k m_u}{\rho_{\text{m},k}}, \quad (9)$$

where \mathcal{A}_k is the molecular weight and $\rho_{\text{m},k}$ the mineral intrinsic density.

The term that describes grain growth and evaporation is written as (GS14, Eqs. (12.101), (12.102), and (12.108))

$$J_{\text{gr},k} - J_{\text{ev},k} = \xi_k \frac{p_j}{\sqrt{2\pi m_j k_B T_g}} \left(\phi_k - \frac{1}{a_k^c} \sqrt{\frac{T_g}{T_d}} \right), \quad (10)$$

where ξ_k is the drift-velocity-dependent sticking coefficient, p_j and m_j are the partial pressure and mass of the rate-determining component, respectively (see Sect. 3.2). Moreover, ϕ_k is the drift correction factor, a_k^c the reaction activity, and T_d the dust temperature.

The sticking coefficient¹ ξ_k is assumed to decrease when the drift velocity becomes high in relation to the binding energy $E_{\text{b},k}$ (Eq. (14) in Krüger & Sedlmayr 1997 and Eq. (13) in Sandin & Höfner 2004, hereafter Paper III).

$$\xi_k = \xi^{(k)} \exp \left[- \left(\frac{\mathcal{A}_k m_u \tilde{w}_k^2}{8E_{\text{b},k}} \right)^3 \right], \quad (11)$$

where the velocity of dust grains relative to gas particles \tilde{w}_k is (Eqs. (11) and (12) in Paper III)

$$\tilde{w}_k = \left(\frac{8k_B T_g}{16\pi \mathcal{A}_k m_u} + \frac{v_{\text{D},k}^2}{16} \right)^{\frac{1}{2}}. \quad (12)$$

Here, $v_{\text{D},k} = v_k - u$ is the drift velocity. Furthermore, the drift correction factor ϕ_k is (Eq. (12.19) in GS14)

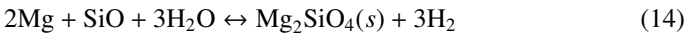
$$\phi_k = \left(1 + \frac{\pi \mathcal{A}_k m_u}{8k_B} \frac{v_{\text{D},k}^2}{T_g} \right)^{\frac{1}{2}}. \quad (13)$$

We use the same expression for non-thermal sputtering ($1/\tau_{\text{sp},n}^k$) as we do in Paper III. Although, here we account for collisions with H_2 molecules, in addition to H and He atoms.

3.2. Growth and evaporation of forsterite

We use two tracer elements: silicon and magnesium. There are in this case eleven equations, instead of thirteen equations when using the moments approach and a carbon-rich chemistry. Forsterite grain growth takes place through collisions of seed grains and extant grains with either SiO molecules or Mg atoms; when addition of SiO (Mg) is the rate determining reaction step, $p_j = p_{\text{SiO}}$ and $m_j = m_{\text{SiO}}$ ($p_j = p_{\text{Mg}}$ and $m_j = m_{\text{Mg}}$).

The basic chemical reaction for forsterite formation, as well as its evaporation through chemical sputtering, is



¹ Please note that in MS21, ξ is used to denote the grain-growth velocity, which is a different, although not unrelated, quantity.

and the (chemical sputtering) reaction activity a_{Fo}^c is (see Eqs. (12.60), (12.103), and (12.104) in GS14)

$$\frac{1}{a_{\text{Fo}}^c} = \frac{p_{\text{H}_2}^3}{p_{\text{SiO}} p_{\text{Mg}}^2 p_{\text{H}_2\text{O}}^3} \frac{K_p(\text{SiO}) K_p^3(\text{H}_2\text{O})}{K_p(\text{Mg}_2\text{SiO}_4) K_p^3(\text{H}_2)}, \quad (15)$$

where the four equilibrium constants K_p are calculated at the dust temperature T_d .

3.3. Partial pressures of atoms and molecules

The number densities of the molecules in the gas phase that are part of the grain formation as well as the activities that determine when dust grains form are calculated in an equilibrium chemistry of molecules with hydrogen, oxygen, carbon, nitrogen, aluminium, silicon, and sulfur, following the approach of GS14 (chapter 10.3). The considered atoms and molecules are: H, H_2 , O, OH, H_2O , CO, CO_2 , CH_4 , N, N_2 , NH_3 , HCN, Al, AlO, AlS, AlOH, AlO_2H , Al_2O , Al_2O_2 , Si, SiO, SiO_2 , S, SO, HS, H_2S , SiS, and S_2 . Magnesium is assumed to be present as free atoms.

All number densities and activities are calculated for the temperature range $100 \leq T_g \leq 10\,000$ K. We use equilibrium constants K_p – that are often referred to as dissociation constants – of Sharp & Huebner (1990), Barklem & Collet (2016), GS14 (see their Table A.5), and NIST JANAF².

4. Modelling procedure and results

We first briefly point at our modelling procedure in Sect. 4.1 and then describe the physics setup and choice of model parameter sets in Sect. 4.2. We present our results in Sect. 4.3.

4.1. Modelling procedure

We follow the modelling procedure described in Sect. 3.1 in Paper V. Due to the low outflow velocity of the wind ($u_\infty \lesssim 10$ km s^{-1}), we set the outer boundary here at $r_{\text{final}}^{\text{ext}} = 20R_\star$. We use $N_d = 840$ grid points, which very nearly corresponds to the grid point arrangement we achieve when using $N_d = 1024$ and $r_{\text{final}}^{\text{ext}} = 40R_\star$. It appears to be sufficient to evolve the wind models for a time interval of about $100P$ (stellar pulsation periods) as the wind structures reach a state of equilibrium before that.

4.2. Physics setup and selection of model parameters

We introduce effects of gas-to-dust drift using one mean dust velocity. We compare the new drift models to PC (non-drift) models that are in all other ways are equivalent to the drift models.

We used solar abundances of Anders & Grevesse (1989), with values for C and O of Grevesse & Sauval (1994). As do B19, we set the pulsation period (P) using the P - L_\star -relation of Whitelock et al. (2009). To correct for too small bolometric variations (Gautschy-Loidl et al. 2004), B19 (see their Sect. 2.2) introduce a free parameter f_L that allows larger variations of the luminosity at the inner boundary. We added the option to T-800 to use a freely chosen value on f_L , and here we use $f_L = 2$, although we note that for our purposes in this paper results of models using either approach are indistinguishable.

² Equilibrium-constant data of NIST/JANAF can be retrieved from <https://janaf.nist.gov/>

Table 1. References of used atom and molecule datasets as well as number of energy levels accounted for in each entry.

molecule	dataset	References	Energy levels
C	Kurucz	1	999
C ₂	8states	2, 3	44 189
C ₂ H ₂	aCeTY	4	5 160 803
CH	MoLLIST	5, 6	2526
CH ₄	YT34to10	7, 8	8 194 057
CN	Trihybrid	9, 10, 11	7703
CO	Li2015	12, 13	6383
CO ₂	UCL-4000	14	3 562 798
CS	JnK	15	11497
CrH	MoLLIST	6	1646
FeH	MoLLIST	16, 6	3564
H ₂	RACPPK	17	302
H ₂ O	POKAZATEL	18	810 269
H ₂ S	AYT2	19	220 618
HCl	HITRAN	20	335
HCN	Harris	21, 22	168 110
HF	Coxon-Hajig	23, 24, 13	684
LaO	BDL	25	38 208
MgH	XAB	26	1303
N	Kurucz	1	283
N ₂	WCCRMT	27, 28, 29	40 380
NH ₃	CoYuTe	30, 31	5 095 730
O	Kurucz	1	201
OH	MoLLIST	32, 33, 6	1878
SO ₂	ExoAmes	34	3 270 270
SiO	SiOUVenIR	35	174 250
SiS	UCTY	36	10 104
TiH	MoLLIST	37	5788
TiO	Toto	38	301 370
VO	VOMYT	39	638 958
YO	SSYT	40	79 440
ZrO	SB	41	3005

References. (1) Kurucz & Bell (1995); (2) Yurchenko et al. (2018b); (3) McKemmish et al. (2020); (4) Chubb et al. (2020); (5) Masseron et al. (2014); (6) Bernath (2020); (7) Yurchenko & Tennyson (2014); (8) Yurchenko et al. (2017); (9) Brooke et al. (2014); (10) Syme & McKemmish (2020); (11) Syme & McKemmish (2021); (12) Li et al. (2015); (13) Somogyi et al. (2021); (14) Yurchenko et al. (2020); (15) Paulose et al. (2015); (16) Dulick et al. (2003); (17) Roueff et al. (2019); (18) Polyansky et al. (2018); (19) Azzam et al. (2016); (20) Gordon et al. (2017); (21) Harris et al. (2006); (22) Barber et al. (2014); (23) Li et al. (2013); (24) Coxon & Hajigeorgiou (2015); (25) Bernath et al. (2022); (26) Owens et al. (2022); (27) Western et al. (2018); (28) Western (2017); (29) Shemansky (1969); (30) Al Derzi et al. (2015); (31) Coles et al. (2019); (32) Brooke et al. (2016); (33) Yousefi et al. (2018); (34) Underwood et al. (2016); (35) Yurchenko et al. (2022); (36) Upadhyay et al. (2018); (37) Burrows et al. (2005); (38) McKemmish et al. (2019); (39) McKemmish et al. (2016); (40) Smirnov et al. (2019); (41) Sorensen & Bernath (2021)

Next, we describe our approach to calculate gas opacities in Sect. 4.2.1, dust properties in Sect. 4.2.2, and our selection of model parameters in Sect. 4.2.3.

4.2.1. Gas opacities

In Paper V, we used tabulated gas opacities $\kappa_{\nu}(\rho_{\text{g}}, T_{\text{g}})$ that were created for carbon-rich chemistries with the COMA code (Aringer

2000; Aringer et al. 2009) for 319 wavenumbers in the interval $400 \leq \tilde{\nu} \leq 39\,480 \text{ cm}^{-1}$, 50 temperatures in the interval $1000 \leq T_{\text{g}} \leq 10\,000 \text{ K}$, and 24 densities in the interval $-18 \leq \log_{10} \rho_{\text{g}} \leq -6 \text{ g cm}^{-3}$.

Here, we calculated new bound-bound gas opacities based on data of the ExoMol project (Tennyson et al. 2020).³ The calculations make use of data for the following 30 atoms and molecules: C, C₂, C₂H₂, CH, CH₄, CN, CO, CO₂, CS, CrH, FeH, H₂, H₂O, H₂S, HCl, HCN, HF, LaO, MgH, N, N₂, NH₃, O, OH, SO₂, SiO, SiS, TiH, TiO, VO, YO, and ZrO, see Table 1. The number of energy levels for each dataset is specified here, however the corresponding number of transitions, or lines, is typically at least an order of magnitude higher. For example, the ExoMol aCeTY C₂H₂ line list has around 5.2 million energy levels and 4.3 billion transitions (Chubb et al. 2021). We used EXOCROSS (Yurchenko et al. 2018a)⁴ to calculate cross sections σ_l for each atom and molecule l at 102 750 wavenumbers in the interval $100 \leq \tilde{\nu} \leq 41\,200 \text{ cm}^{-1}$, 105 temperatures in the interval $100 \leq T_{\text{g}} \leq 10\,000 \text{ K}$, and 24 gas densities in the interval $-18 \leq \log_{10} \rho_{\text{g}} \leq -6 \text{ g cm}^{-3}$. The cross sections are resampled to a coarse grid of a pre-defined set of wavenumbers, where the resulting cross section is the average of the ten nearest cross sections on the finer grid. Currently, we used 384 wavenumbers; this is an even multiple of the number of cores available on each node (2×64) on a current high-performance cluster we used. Individual cross sections are thereafter converted to bound-bound opacities by multiplying with the corresponding partial pressure p_l as

$$\kappa_{\text{bb},l} = \frac{p_l}{k_{\text{B}} T_{\text{g}} \rho_{\text{g}}} \left[\text{cm}^2 \text{g}^{-1} \right]. \quad (16)$$

We calculated partial pressures for the 27 molecules listed above as well as the three individual atoms using the same approach as in Sect. 3.3.

Bound-bound opacities become low at higher temperatures ($T_{\text{g}} \gtrsim 2000 \text{ K}$), where instead bound-free opacities κ_{bf} and free-free opacities κ_{ff} dominate. We calculated such opacities using the JEKYLL code (Ergon et al. 2018; Ergon & Fransson 2022), see Appendix A for more information.

Finally, bound-bound and bound-free opacities of individual atoms, molecules, and ions as well as free-free opacities of ions are summed up to provide a total abundances-dependent gas opacity for each pair of gas density and gas temperature,

$$\kappa_{\nu}(\rho_{\text{g}}, T_{\text{g}}) = \sum_l \kappa_{\text{bb},l} + \sum_i (\kappa_{\text{bf},i} + \kappa_{\text{ff},i}).$$

Each set of abundances-specific opacities are saved in a binary file tabulated in wavenumber, density, and temperature. The opacities are interpolated in density and temperature for each individual wavenumber in the radiative transfer calculations using two-dimensional rational splines (Späth 1995).

We were at first kindly provided with the same opacity table for solar metallicities that B19 use (Aringer, priv. comm.). Due to unknown reasons, we were unsuccessful in using these data with our new models. We discuss these extant opacity data and make a simple comparison with our new opacities in Appendix B.

4.2.2. Dust properties

We list all forsterite-specific dust parameters we used in Table 2. We illustrate how the sticking coefficient ξ_k varies with the drift

³ <https://www.exomol.com/>.

⁴ <https://github.com/ExoMol/ExoCross>.

Table 2. Dust parameters: forsterite

parameter	value	B19 ^a	unit	Reference
ϵ_{Fo}	10^{-15}	10^{-15}		1
\mathcal{A}_{Fo}	140.694	140		2, 3
$\rho_{\text{m,Fo}}$	3.21	3.27	g cm^{-3}	2, 3
ξ_{Fo}	0.1	1.0		4
$E_{\text{b,Fo}}$	3.5	–	eV	5
$\nu_{\text{Fo}}^{\text{Si}}, \nu_{\text{Fo}}^{\text{Mg}}$	1, 2 ^b	1, –		

References. (1) B19; (2) Lide (1995); (3) GS14, Table 12.1; (4) GS14, Sect. 12.7.1; (5) Barlow (1978), the ‘‘Silicate’’ entry in Table 4

Notes.^a The values we assume B19 use are specified by Höfner et al. (2016). ^b For all elements j , but Mg and Si, $\nu_{\text{Fo}}^j = 0$.

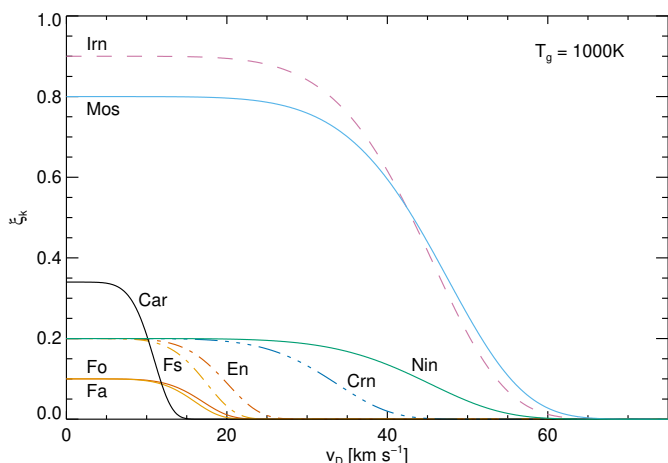


Fig. 3. The sticking coefficient ξ_i (Eq. (11)) versus the drift velocity v_D for nine different minerals, assuming a gas temperature $T_g = 1000$ K.

velocity for forsterite and eight other minerals in Fig. 3 (cf. Fig. 1 in Paper III); the parameters of the eight additional minerals are taken from the same set of references as for forsterite, noting that the binding energies of several minerals are highly uncertain. The figure shows that the sticking coefficient drops to 0 when $v_D \gtrsim 20$ km s^{-1} for larger mineral monomers such as forsterite (Fo), fayalite (Fa), enstatite (En), and ferrosilite (Fs) and also for carbon (Car; amorphous carbon or graphite). Higher velocities are possible with corundum (Crn; $v_D \approx 40$ km s^{-1}) as well as iron (Irn), moissanite (Mos), and niningerite (Nin) where the cut-off drift velocity is about 60 km s^{-1} . Hence, there is for forsterite no grain growth when the drift velocity is higher than 20 km s^{-1} .

All models were calculated using Mie scattering. Optical constants (n_v , k_v) are taken from Jäger et al. (2003).⁵ To achieve results comparable with B19, we used the seed particle abundance $\epsilon_{\text{Fo}} = 10^{-15}$ with all our calculations, as well as the same sticking coefficient with our PC models, $\xi^{(\text{Fo})}(\text{PC}) = 1.0$.

4.2.3. Selection of model parameters

Our new model calculations of M-star objects are as demanding as those of C stars in Paper V. Initial results of our new M-type wind models have indicated drastically lower mass-loss rates in our current forsterite-driven drift models, which is why we found it necessary to select stellar parameter sets similar to non-drift

⁵ The optical data can be retrieved from <https://www.astro.uni-jena.de/Laboratory/OCDB/amsilicates.html>.

Table 3. Model parameters. Six columns specify the: model setup name, stellar mass M_\star , stellar luminosity L_\star , effective temperature T_{eff} , pulsation amplitude Δu_p , and luminosity-dependent pulsation period P .

model	M_\star [M_\odot]	$\log(L_\star)$ [L_\odot]	T_{eff} [K]	Δu_p [km s^{-1}]	P [d]
L3.85T24	1.00	3.85	2400	3.0	478
L3.85T27	1.00	3.85	2700	4.0	478
L4.30T29	1.00	4.30	2900	4.0	1060
L4.45T29	1.50	4.45	2900	4.0	1376

simulations where results are known to give high mass-loss rates. Here we calculated four sets of models to get a first impression of how the formation of stellar winds of M stars work when the dust component is allowed to drift relative to the gas. All model parameters are collected in Table 3.

Our focus was to vary the temperature and luminosity; this also sets the period (see Sect. 4.2). We used a higher value with the piston amplitude as such a value is more likely to result in the formation of a stellar wind using drift. There is little reason to fine tune this amplitude currently considering all other – still – imprecise factors of these new models. Finally, we use the same value on the stellar mass, $M_\star = 1 M_\odot$, with the exception of the model with the highest luminosity where we use $M_\star = 1.5 M_\odot$ (see below).

At first, we selected the proof-of-concept-model set B of H08 ($\log(L/L_\odot) = 3.85$, $T_{\text{eff}} = 2700$ K), which she uses to illustrate that dust-driven winds also form in M-type stars when Mie scattering is used in the description of dust extinction instead of the SPL approximation. Secondly, we selected a model set of B19 with a lower effective temperature that is also found to form a higher mass-loss rate ($\log(L/L_\odot) = 3.85$, $T_{\text{eff}} = 2400$ K).

Marini et al. (2023) consider a small sample of AGB stars – observed with the Atacama Large Millimeter Array (ALMA) – that show spectral energy distributions of amorphous silicates characterised by deep absorption features at 10 and 18 μm . Based on their observed properties and evolutionary tracks, we find it valuable to also consider a higher effective temperature using a lower and higher luminosity. Consequently, we added a third set with $\log(L/L_\odot) = 4.30$, $T_{\text{eff}} = 2900$ K, and $M_\star = 1.0 M_\odot$, as well as a fourth set with $\log(L/L_\odot) = 4.45$, $T_{\text{eff}} = 2900$ K, and $M_\star = 1.5 M_\odot$. The latter setup corresponds, roughly, to a mass-loss peak in the evolutionary track with initial mass $M = 6 M_\odot$ in Marini et al. (2023). The former setup is a compromise to capture mass-loss characteristics of the $M = 4 M_\odot$ and $M = 5 M_\odot$ tracks.

4.3. Results

As in Paper V, we characterize wind models with a set of properties that are temporally averaged at the outer boundary. The mass loss rate $\langle \dot{M} \rangle$ and the terminal velocity $\langle u_\infty \rangle$ characterize the gas. The degree of condensation of silicon $\langle f_{\text{cond}}^{\text{Si}} \rangle$ and magnesium $\langle f_{\text{cond}}^{\text{Mg}} \rangle$, the dust-to-gas mass-loss ratio $\langle \dot{M}_d / \dot{M} \rangle$, the mean grain radius $\langle r_d \rangle$, and the terminal drift velocity $\langle v_{D,\infty} \rangle$ characterize the dust.

The drift-velocity dependent [true] degree of condensation of tracer element j accounting for all minerals k is calculated as

Table 4. Temporally averaged quantities at the outer boundary, see Section 4.3. From the left, the first three columns specify the model name (see Table 3), if PC or drift is used (P/D), and the sticking coefficient ($\xi^{(F0)}$). Nine column pairs show the temporally averaged: mass loss rate (\dot{M}), terminal velocity ($v_{D,\infty}$), modified ($f_{\text{cond}}^{\text{Mg}}$) and true ($f_{\text{cond}}^{\text{Si}}$) degrees of condensation of silicon, modified ($f_{\text{cond}}^{\text{Mg}}$) and true ($f_{\text{cond}}^{\text{Si}}$) degrees of condensation of magnesium, dust-to-gas mass-loss ratio ($\delta_{\text{dg}} \delta_{\text{D}}^{\text{co}}$), and dust radius (a_{F0}). A relative fluctuation amplitude \hat{r} is provided for each property; a subscript m indicates that the shown value was multiplied with a factor 10^3 . All values are indented to make visible the large variation of values of each property across all models. The final columns show the outflow classification class: periodic (P), and quasi-periodic (Q); / indicates the (multi-)periodicity of the gas/dust outflow in the unit of the piston period P . Rows of drift models are shown in boldface.

model	P/D	$\xi^{(F0)}$	$10^8 \langle \dot{M} \rangle$ [$M_{\odot} \text{ yr}^{-1}$]	$\langle u_{\infty} \rangle$ [km s^{-1}]	$\langle v_{D,\infty} \rangle$ [km s^{-1}]	$\langle \tilde{f}_{\text{cond}}^{\text{Si}} \rangle$ \hat{r}	$\langle f_{\text{cond}}^{\text{Si}} \rangle$ \hat{r}	$\langle \tilde{f}_{\text{cond}}^{\text{Mg}} \rangle$ \hat{r}	$\langle f_{\text{cond}}^{\text{Mg}} \rangle$ \hat{r}	$10^4 \langle \delta_{\text{dg}} \delta_{\text{D}}^{\text{co}} \rangle$ \hat{r}	$10^2 \langle a_{F0} \rangle$ [μm]	cl.	
L3.85T24	P	1.0	218	11.1	0.17	0.184	40 _m	0.344	74 _m	6.62	1.4	48.2	3.6
	P	0.1	32.8	4.89	42 _m	0.127	3.0 _m	0.238	5.7 _m	4.58	0.11	42.8	0.34
B19	P	1.0	248	10.0		0.18		0.18		6.49		48	
	D	1.0	1.6	0.16	297	0.327	0.12	0.611	0.22	278	110	57.9	6.3
	D	0.1	3.8	0.38	194	0.294	0.18	0.549	0.33	173	117	55.0	9.2
L3.85T27	P	1.0	19.4	4.64	80 _m	0.125	11 _m	0.233	21 _m	4.48	0.40	42.5	1.2
H08-B	P	1.0	80	7		0.15		0.15				45	
B19	P	1.0	362	9.2		0.15		0.15		5.20		45	
	D	0.1	1.21	0.21	313	0.290	0.17	0.542	0.33	296	190	54.3	11
L4.30T29	P	1.0	663	7.70	1.3	88.7 _m	46 _m	0.165	86 _m	3.18	1.7	35.8	9.5
	D	0.1	631	0.49	13.0	77.0_m	85_m	0.144	0.16	8.76	11	32.6	11
L4.45T29	P	1.0	278	5.17	0.12	56.7 _m	5.3 _m	0.106	9.9 _m	2.04	0.19	32.7	1.0
	D	0.1	35.5	9.87	86.7	89.3_m	54_m	0.167	0.10	35.1	30	36.8	6.5

(cf. Eq. (12.81) in GS14⁶ and Eq. (33) in Paper V)

$$f_{\text{cond}}^j = \sum_k \frac{4\pi a_j^3}{3} \frac{1}{V_{1,j}} \frac{1}{\tilde{\nu}_{D,k}} \frac{\epsilon_k \nu_k^j}{\epsilon_j} = \frac{1}{\epsilon_j} \sum_k \frac{N_k \epsilon_k \nu_k^j}{\tilde{\nu}_{D,k}}, \quad (17)$$

where $\tilde{\nu}_{D,k} = 1 + |v_{D,k}| / (|u| + \epsilon_u)$ is the drift factor,⁷ where we use $\epsilon_u = 0.1 \text{ km s}^{-1}$. The variable ϵ_j is the abundance of element j . In PC models, the modified degree of condensation is (cf. Eq. (12.85) in GS14)

$$\tilde{f}_{\text{cond}}^j = \frac{1}{\epsilon_j} \sum_k N_k \epsilon_k \nu_k^j. \quad (18)$$

Whilst the true degree of condensation corresponds to the modified degree of condensation diluted by the relative velocity of dust to gas, we also present modified degrees of condensation for drift models as these values illustrate the more efficient dust-formation process in drift models. Moreover, the dust-to-mass mass-loss ratio is

$$\frac{\dot{M}_d}{\dot{M}} = \sum_k \frac{\rho_{d,k}}{\rho_g} \frac{v_{\infty,k}}{u_{\infty}} = \sum_k \delta_{d,g,k} \tilde{\nu}_{D,k}^{\infty}, \quad (19)$$

where $\delta_{d,g,k} = \rho_{d,k} / \rho_g$.

We calculated a relative fluctuation amplitude \hat{r} for each property Q as $\hat{r} = \sigma_s / Q$, where σ_s is the (sample) standard deviation of the property Q in the time interval that is used to measure the same property. We show results of our model calculations in Table 4.

5. Discussion

We analyse the new results of our PC models in Sect. 5.1 and then compare PC models with our new drift models in Sect. 5.2.

5.1. Comparing results of the PC (non-drift) models

5.1.1. The lower temperature model L3.85T24

Our PC models using a unity sticking coefficient ($\xi^{(\text{Fo})} = 1.0$) reveal a more massive wind than when $\xi^{(\text{Fo})} = 0.1$. The mass-loss rate and expansion velocity are 5.6 and 1.3 times higher, respectively. A lower ratio of 1.4 is seen in the degree of condensation and the dust-to-gas density ratio. The average grain radius is 13 % higher. Fluctuation amplitudes are 3–12 times higher in all values, but the mass-loss rate, where it is 62 times higher. Clearly, a unity sticking coefficient results in a more variable wind where all values but the grain radius are higher, but the increase is with the exception of the mass-loss rate 13–130 % and not a factor 10.

In comparison to B19, and assuming a unity sticking coefficient, our values on the degrees of condensation and dust-to-gas density ratio are 2.0–2.2 % higher, the grain radius 0.42 % higher and the mass-loss rate 12 % lower. These values compare well.

⁶ We ignore the seed particle radius $a_{0,j}$ used by GS14, noting that the contribution of seed particles to the degree of condensation is miniscule already at small particle radii a_j that are barely larger than $a_{0,j}$.

⁷ This form of the drift factor allows calculation of the degree of condensation also when the sign of the gas and dust velocity components differ, which could be the case in the radial region where the stellar wind first forms in time-dependent simulations.

5.1.2. The proof-of-concept model L3.85T27

H08 presents model L3.85T27 (“model B”) as a proof of the concept that scattering on larger dust particles in place of absorption allows formation of massive stellar winds in M-type stars. B19 calculate a model with the same stellar parameters, also with 100 grid points, but use a somewhat longer pulsation period ($P = 478 \text{ d}$, instead of $P = 390 \text{ d}$) and also favour a lower pulsation amplitude ($\Delta u_p = 2 \text{ km s}^{-1}$). We used the same stellar parameters as B19, where $\Delta u_p = 4 \text{ km s}^{-1}$. We also set the sticking coefficient to unity, but we used a higher spatial resolution achieved with $N_D = 840$ grid points. We show the resulting values of both H08 and B19 in Table 4 for easy reference.

Our new values on the silicon degree of condensation and the mean grain radius agree well with these two studies; our values are 83 % and 94 % of their values, respectively. Similarly, our value on the dust-to-gas ratio is 86 % of the value of B19. Regarding the mass-loss rate and expansion velocity, our values are 24 % and 66 % (5.4 % and 50 %) of the values of H08 (B19). Our mass-loss rate is, obviously, closer to the value of H08, whilst the difference is much larger in comparison to B19. Notably, the agreement with B19 is not as close as in model L3.85T24. In any case, the agreement depends on where exactly the inner boundary is located, as that determines the amount of mass in the model domain. As neither B19 nor other authors specify the location of the inner boundary or the mass in the model domain, there is some arbitrariness to the agreement of results; this also applies to model L3.85T24 above.

5.1.3. The two higher temperature models L4.30T29 and L4.45T29

Model L4.30T29 shows the highest mass-loss rate of all four PC models, with associated large variabilities. The expansion velocity remains low. The degree of condensation is about half the value of models L3.85T24 and L3.85T27; this is also reflected in the dust-to-gas mass-loss ratio. The mean grain size is somewhat lower than in the first two models.

Model L4.45T29 is modelled using both a higher mass and a higher luminosity than L4.30T29. The results show a mass-loss rate that is 58 per cent lower. The remaining properties of the more luminous model are 33–36 % lower. The exception is the average grain size, which is 8.7 % lower. Compared to the same model, relative fluctuation amplitudes of the mass-loss rate are 4.6 % and the remaining properties 9.2–12 %. It is clear that the higher luminosity does not compensate for the higher gravitational pull owing to the higher stellar mass. It is noteworthy that both luminous model setups result in high mass-loss rates, whilst forming smaller amounts of dust than in models L3.85T24 and L3.85T27.

5.2. Comparing results of the drift models

5.2.1. L3.85T24: Effects of the sticking coefficient

The drift model shows a different result in comparison to the PC model L3.85T24 – the values of the two drift models are similar when comparing properties that do not depend on the dust velocity (they differ by 5.3–15 %), with the exception of the mass-loss rate where the value of the unity sticking coefficient model is 42 % lower than in the other model. Due to the 53 % higher drift velocity of the unity sticking coefficient model, the dust-to-gas mass loss rate ratio differs by 61 %, and the true degrees of condensation by –23 %. Thus, the model with the lower sticking

coefficient results in a much higher mass loss. A plausible explanation to this is that less efficiently formed dust grains can flow to regions where they more effectively contribute to wind formation, before there is enough dust to accelerate both the dust and gas outwards. Notably, the very high drift velocity of 194 km s^{-1} increases by 53% to 297 km s^{-1} in the unity model. The true degrees of condensation are a factor 15–22 lower than the modified degrees of condensation owing to the high drift velocities. The fluctuation amplitudes are, finally, all very similar (they differ by -58 – 27 %).

We compare the drift model using $\xi^{(\text{Fo})} = 0.1$ with our PC model where $\xi^{(\text{Fo})} = 1.0$. The mass-loss rate of the drift model is 1.7 %, the dust-to-gas density ratio 2600 %, and the true degrees of condensation 9.9 % of the corresponding values of the PC model. The differences are much smaller in the expansion velocity (18 % higher) and the grain radius (14 % higher). The same comparison with the model of B19 gives a mass-loss rate that is 1.5 %, a dust-to-gas density ratio that is 2700 %, and a degree of condensation of silicon 10 % of their values. Similarly, differences are smaller in the expansion velocity (30 % higher) and the grain radius (15 % higher). The huge increase in the dust-to-gas density ratio of the drift model must be put in context of the drastically lower mass-loss rate; dust forms more efficiently, whilst the wind formation efficiency is lower. Nevertheless, the differences in comparison to the PC models of about a factor 1/50 in the mass-loss rate and a factor 26 in the dust-to-gas density ratio are large and must not be ignored.

5.2.2. The proof-of-concept drift model L3.85T27

The values of the drift model again differ from our PC model. The mass-loss rate is here 94 % lower, the dust-to-gas density ratio 65 times higher, and the degrees of condensation 92 % lower. Furthermore, the expansion velocity is 160 % higher, and the mean grain radius 28 % higher. Temporal fluctuations are higher in the dusty properties, but the fluctuations are generally low. Both the drift model and the PC model show quasi periodic variations. The mass-loss rate is 0.33 % of the value of B19, the dust-to-gas density ratio 56 times higher, and the degree of condensation of silicon is 7 % of the value of B19. The expansion velocity is 29 % higher and the grain radius 21 % higher.

We plot our PC and drift models versus the radius in Fig. 4. The inefficient mass loss of the drift model is seen in the gas density that is a hundred times lower than in the PC model (Fig. 4b). Despite the lower mass-loss rate, the expansion velocity of the drift model is more than twice as high than in the PC model, see Fig. 4a. The gas opacity κ_{H} increases somewhat towards higher radii (Fig. 4j), whilst the Rosseland mean opacity κ_{R} decreases to be a millionth and less of κ_{H} at higher radii; notably, the same ratio is closer to a factor ten in the carbon-rich model shown in Fig. 8j in Paper V. The Eddington factor of both models (Fig. 4g) indicates that there is no need to solve the equation of radiative transfer where $R \gtrsim 10 R_{\star}$, as the factor is very close to unity.

The drift velocity shown in Fig. 4c attains high values already near the star. The same high values cause an abrupt cut-off in the dust formation rates at radii $r \gtrsim 3 R_{\star}$ (Fig. 4e). The same panel illustrates that, despite the high drift velocity, non-thermal sputtering ($\tau_{\text{sp,n}}^{-1}$) is negligible at all radii owing to the low gas density. The [true] degree of condensation (Fig. 4d) and extinction coefficient (Fig. 4h) are significantly lower in the drift model.

The dust-to-radiative temperature ratio in Fig. 4k shows a value that is the inverse of the same ratio in a stellar wind of a carbon star (cf. Fig. 8k in Paper V). The forsterite dust temper-

ature is always lower than the radiative temperature; it is about half as high in the outer regions. In comparison, the amorphous carbon dust temperature is always higher than the radiative temperature; and it is up to about 50 % higher in the outer regions. No other indicator illustrates the difference as clearly between scattering and absorption dominated dust extinction.

5.2.3. The two higher temperature models L4.30T29 and L4.45T29

The drift and PC models L4.30T29 show results that are very similar. This similarity is owing to the drift velocity, $v_{\text{D}} = 13 \text{ km s}^{-1}$, which is drastically lower than in the other three drift models of this study. Comparing the other values, the mass-loss rate is 4.8 % lower, the expansion velocity 1.7 % higher, the modified degrees of condensation 13 % lower, the true degrees of condensation 71 % lower, the dust-to-gas mass-loss ratio 180 % higher, and the average grain size 8.9 % lower. The relative fluctuation amplitude of the dust-to-gas mass-loss ratio and average grain size are 550 % and 16 % higher, respectively. The same values of the modified degrees of condensation are 85–86 % higher. The fluctuation amplitudes of all remaining properties are 48–73 % lower.

This model setup shows a similarly strong stellar wind for an M-type star as the models of the C-type star IRC 10²216 discussed in Andersson et al. (2022), which is modelled using an even less massive star. Also, of the models discussed here, this is the only setup where a comparatively smaller amount of forsterite is able to drive a more massive wind.

Model L4.45T29 shows a drift velocity that is 5.7 times higher compared to model L4.30T29, and the mass-loss rate of the former model is 5.6 % of the latter one. Comparing the values of the drift model with those of the PC model, the mass-loss rate is 13 %, the expansion velocity 91 % higher, the modified degrees of condensation 57 % higher, the true degrees of condensation 58 % lower, the dust-to-gas mass-loss ratio 16 times higher, and the average grain size 13 % higher. The relative fluctuation amplitude of the dust-to-gas mass-loss ratio and average grain size are 157 and 5.5 times higher, respectively. The same values of the modified degrees of condensation are 9 times higher. The fluctuation amplitude of the mass-loss rate is 8.4 % of the PC model value. And the fluctuation amplitude of the expansion velocity and the true degrees of condensation are 23 % and 40–42 % lower.

As in the PC model, the higher stellar mass of this setup cancels the effect of the higher luminosity. In accordance with model L4.30T29 and despite a smaller amount of dust, this model also forms a more massive wind than do models L3.85T24 and L3.85T27.

5.2.4. Implications of allowing gas-to-dust drift

For all four presented model setups, the measured expansion velocity of the drift model is higher than that of the corresponding PC model. The mass-loss rate of the drift model is, at the same time, lower to drastically lower. This result could be taken as a sign of stellar wind formation in an O-rich chemistry of an M-type star when one compares with the models of C-type stars in Paper V, where the same result holds for only six out of 22 model setups. For example, the gas density of model setups L3.85T24 and L3.85T27 is lower by about a factor 100 in the drift model compared to the PC model, see Fig. 4b for the latter setup. In these two cases of extremely low drift model gas densities and

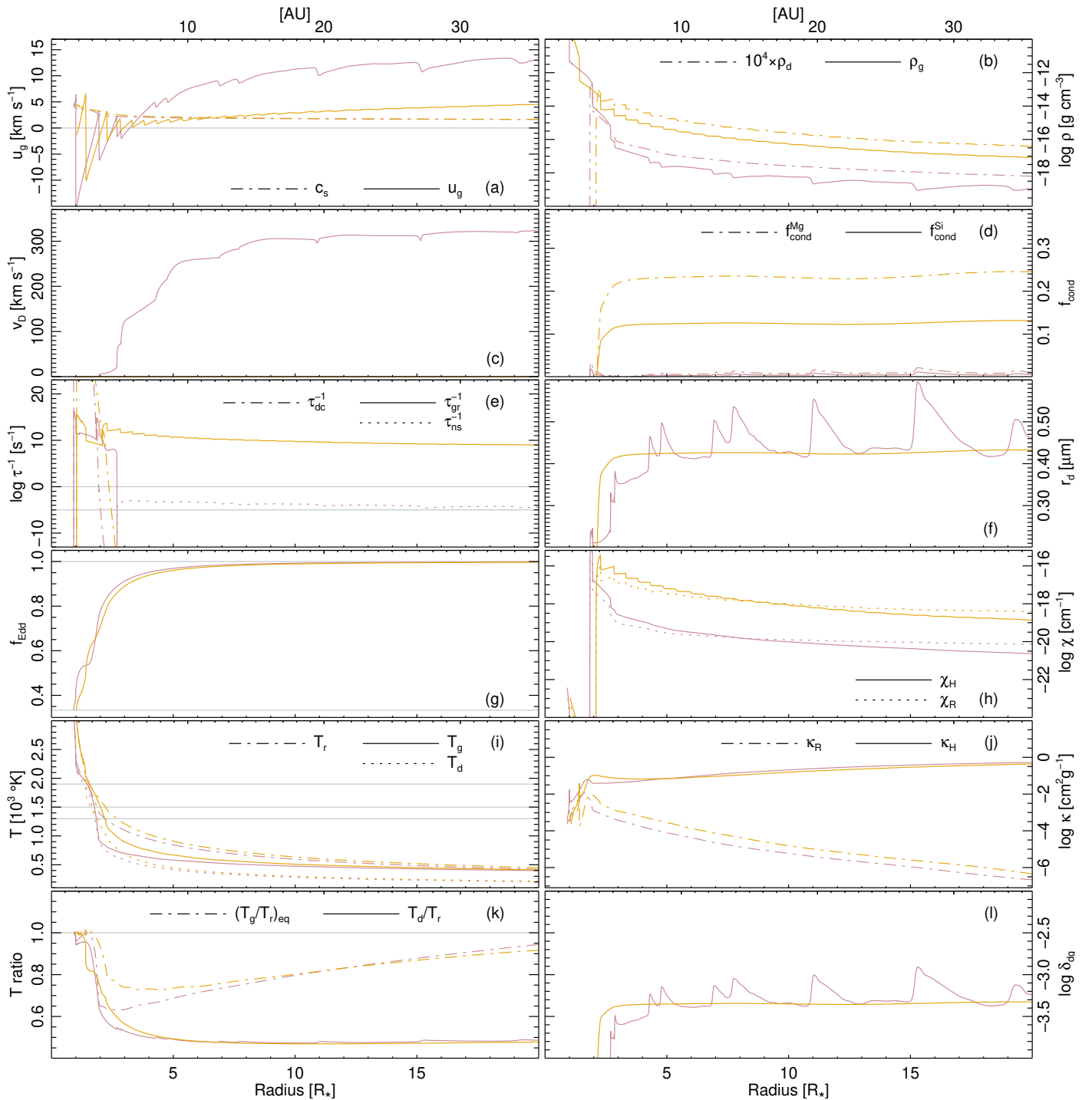


Fig. 4. Radial structure of a snapshot of setup L3.85T27 for the full modelled region. The drift model (where $\xi^{(\text{Fo})} = 0.1$; PC model, where $\xi^{(\text{Fo})} = 1.0$) is shown with purple (orange) lines. From the top left, the 12 panels show: (a) gas velocity u_g , sound speed c_s ; (b) gas density ρ_g , dust density $10^4 \times \rho_d$ (log); (c) drift velocity v_D ; (d) [true] degree of condensation of silicon $f_{\text{cond}}^{(\text{Si})}$ and magnesium $f_{\text{cond}}^{(\text{Mg})}$; (e) net growth rate τ_{gr}^{-1} , net decay rate τ_{dc}^{-1} , non-thermal sputtering τ_{ns}^{-1} (log) times $n_{\text{d,Fo}} dV$ (where dV is the cell volume); (f) average grain radius r_d ; (g) Eddington factor f_{Edd} ; (h) extinction coefficient χ_H , Rosseland mean extinction coefficient χ_R ; (i) gas temperature T_g , radiative temperature T_r , and dust temperature T_d ; (j) gas opacity κ_H and Rosseland mean opacity κ_R (log); (k) temperature ratios T_d/T_r and $(T_g/T_r)_{\text{eq}}$; and (l) dust-to-gas density ratio δ_{dg} . All properties are drawn versus the stellar radius R_* (lower axis) and astronomical units (AU; upper axis). Grey horizontal lines are guides.

mass-loss rates, it is clear that the expansion velocity of the drift models can be higher based on the argument that it is easier to accelerate the gas (and thereby the wind) when the gas density is lower. However, when mass-loss rates of drift and PC models using the same model setup are more similar, there is no unambiguous evidence for this being a rule that applies to all winds of

M-type stars. For example, the differences in expansion velocities and mass-loss rates is smaller with model setup L4.30T29.

The differences between results of the four drift models and the corresponding PC models presented here are with one exception enormous. Our values on the mass-loss rates of the PC models are 56, 15, and 6.8 times higher than the corresponding drift

model. The exception is model L4.30T29 where the difference is only 10%. These values grow to 64 and 300 times when we instead compare with the corresponding values of B19 for the two less luminous model setups. And the mass-loss rate of the proof-of-concept model of H08 is 65 times higher than in our drift model. Besides different model parameters and modeling approach, the differences are owing to the scattering-dominated dust extinction of forsterite, which results in extraordinarily high drift velocities. In the exception model, this does not appear to be the case. Here, with a high luminosity and a lower stellar mass, it is only necessary to form small amounts of dust to drive a massive wind. High drift velocities imply that any features in the diluted dust component in observations will be minuscule. More reliable observations of mass loss based on radio observations of CO, which make fewer assumptions on the dust component, indicate that mass-loss rates are high – evidently something is needed to achieve these high mass-loss rates also in simulations. An unidentified component that is not yet included in our models.

The question is what happens when additional dust species are added to the simulations. Not all species are as transparent as forsterite. It seems valuable to study changes in the radiation field and wind driving mechanism where also enstatite is added and species that include iron, such as fayalite and ferrosilite and thereby olivine and pyroxene as well as corundum and pure iron dust. Bladh & Höfner (2012) and also GS14 (see Chapter 12) argue that these minerals form much farther out than iron-free minerals, but it is still unknown what the result will be in a multi-fluid model where temperature gradients of drift models may be much steeper in the inner wind forming region (see Fig. 4i). Drift must not be ignored in stellar winds that are driven by minerals such as forsterite where extinction is dominated by scattering.

6. Conclusions

We have extended our frequency-dependent dust-driven high-spatial-resolution wind model code T-800 of Paper V with descriptions for mineral formation in oxygen-rich chemistry, as laid out by GS14. We have also calculated new opacity tables that are based on bound-bound cross sections of thirty [atoms and] molecules of the ExoMOL project and free-free and bound-free opacities of the JEKYLL code. With our improved model code and opacity data, we can choose molecular compositions and wavelengths freely and model stellar winds of both C-type and M-type stars that form various types of minerals. To our understanding, T-800 is the physically and numerically most detailed dynamic stellar wind code there is, and it is the only one that can accurately calculate effects of gas-to-dust drift in either type of star.

We have calculated models to explore effects of drift in M-type winds that are driven by forsterite particles. Extant studies favour this species as a wind driver. We selected model parameter setups that are expected to and have shown high mass-loss rates. Our new PC models show a good comparison with extant results (of H08 and B19); we cannot be more specific as details of those extant simulations are unavailable in the literature.

Differences are much larger when we compare results of PC models with drift models. Whilst changes in expansion velocities and grain sizes are modest, this is not so for the degree of condensation, dust-to-gas density ratio, and mass-loss rates. The drift velocity is with one exception 87–310 km s⁻¹ in the presented models; these high values result in very low degrees of condensation. One luminous model shows a lower drift velocity of 13 km s⁻¹, which is still about twice as high as the expansion

velocity of the same model. The mass-loss rate is 1.7–13% of the PC model value. In the one exception model, the same value is 95%. One of the models showing larger differences (L=7080L_⊙, T=2700K) is important as H08 use a model with the same parameters to prove the concept of stellar wind formation in M-type stars. Drift is more important in M-type stars than in C-type stars – the biggest difference is that momentum is transferred from the radiation field to the dust grains through scattering on transparent grains instead of through absorption in opaque grains.

More studies are needed that explore the use of simultaneous formation of additional dust species to explain how observed high mass-loss rates form. And this cannot be done without drift – the resulting simulations are a multi-fluid problem. This article is a proof of concept of the influential effects of drift. Our analysis and results show that effects of drift on stellar wind of AGB stars are strong and that they cannot be correctly determined when drift is ignored.

Acknowledgements. K.L.C. acknowledges funding from STFC, under project number ST/V000861/1. Most of the computations were enabled by resources provided by the Swedish National Infrastructure for Computing (SNIC), partially funded by the Swedish Research Council through grant agreement no. 2018-05973. We thank B. Aringer (Vienna and Padova) for kindly providing us with an opacity table that we could use to develop and test our new model.

References

- Al Derzi, A. R., Furtenbacher, T., Tennyson, J., Yurchenko, S. N., & Császár, A. G. 2015, *J. Quant. Spectr. Rad. Transf.*, 161, 117
- Anders, E. & Grevesse, N. 1989, *Geochim. Cosmochim. Acta*, 53, 197
- Andersson, B. G., Lopez-Rodriguez, E., Medan, I., et al. 2022, *ApJ*, 931, 80
- Aringer, B. 2000, PhD thesis, Universität Wien
- Aringer, B., Girardi, L., Nowotny, W., Marigo, P., & Lederer, M. T. 2009, *A&A*, 503, 913
- Azzam, A. A. A., Tennyson, J., Yurchenko, S. N., & Naumenko, O. V. 2016, *MNRAS*, 460, 4063
- Barber, R. J., Strange, J. K., Hill, C., et al. 2014, *MNRAS*, 437, 1828
- Barklem, P. S. & Collet, R. 2016, *A&A*, 588, A96
- Barlow, M. J. 1978, *MNRAS*, 183, 367
- Bernath, P. F. 2020, *J. Quant. Spectr. Rad. Transf.*, 240, 106687
- Bernath, P. F., Dodangodage, R., & Liévin, J. 2022, *ApJ*, 933, 99
- Bladh, S. & Höfner, S. 2012, *A&A*, 546, A76
- Bladh, S., Höfner, S., Aringer, B., & Eriksson, K. 2015, *A&A*, 575, A105
- Bladh, S., Höfner, S., Nowotny, W., Aringer, B., & Eriksson, K. 2013, *A&A*, 553, A20
- Bladh, S., Liljegren, S., Höfner, S., Aringer, B., & Marigo, P. 2019, *A&A*, 626, A100 (B19)
- Blommaert, J. A. D. L., de Vries, B. L., Waters, L. B. F. M., et al. 2014, *A&A*, 565, A109
- Bohren, C. F. & Huffman, D. R. 1983, *Absorption and scattering of light by small particles* (Wiley, New York)
- Brooke, J. S. A., Bernath, P. F., Western, C. M., et al. 2016, *J. Quant. Spectr. Rad. Transf.*, 168, 142
- Brooke, J. S. A., Ram, R. S., Western, C. M., et al. 2014, *ApJS*, 210, 23
- Burrows, A., Dulick, M., Bauschlicher, C. W., J., et al. 2005, *ApJ*, 624, 988
- Chubb, K. L., Rocchetto, M., Yurchenko, S. N., et al. 2021, *A&A*, 646, A21
- Chubb, K. L., Tennyson, J., & Yurchenko, S. N. 2020, *MNRAS*, 493, 1531
- Coles, P. A., Yurchenko, S. N., & Tennyson, J. 2019, *MNRAS*, 490, 4638
- Coxon, J. A. & Hajigeorgiou, P. G. 2015, *J. Quant. Spectr. Rad. Transf.*, 151, 133
- Dorschner, J. 2010, in *Lecture Notes in Physics*, Berlin Springer Verlag, ed. T. Henning, Vol. 815, 1–60
- Dulick, M., Bauschlicher, C. W., J., Burrows, A., et al. 2003, *ApJ*, 594, 651
- Ergon, M. & Fransson, C. 2022, *A&A*, 666, A104
- Ergon, M., Fransson, C., Jerkstrand, A., et al. 2018, *A&A*, 620, A156
- Gail, H.-P. & Sedlmayr, E. 1999, *A&A*, 347, 594
- Gail, H.-P. & Sedlmayr, E. 2014, *Physics and Chemistry of Circumstellar Dust Shells*, 52 (Cambridge Univ. Press, New York) (GS14)
- Gautschy-Loidl, R., Höfner, S., Jørgensen, U. G., & Hron, J. 2004, *A&A*, 422, 289
- González Delgado, D., Olofsson, H., Kerschbaum, F., et al. 2003, *A&A*, 411, 123
- Gordon, I. E., Rothman, L. S., Hill, C., et al. 2017, *J. Quant. Spectr. Rad. Transf.*, 203, 3

- Grevesse, N. & Sauval, A. J. 1994, in IAU Colloq. 146: Molecules in the Stellar Environment, ed. U. G. Jorgensen, Vol. 428, 196–208
- Harris, G. J., Tennyson, J., Kaminsky, B. M., Pavlenko, Y. V., & Jones, H. R. A. 2006, *MNRAS*, 367, 400
- Höfner, S. 2008, *A&A*, 491, L1 (H08)
- Höfner, S., Bladh, S., Aringer, B., & Ahuja, R. 2016, *A&A*, 594, A108
- Höfner, S. & Olofsson, H. 2018, *A&A Rev.*, 26, 1
- Hubeny, I. & Mihalas, D. 2015, *Theory of Stellar Atmospheres* (Princeton Univ. Press, Princeton)
- Jäger, C., Dorschner, J., Mutschke, H., Posch, T., & Henning, T. 2003, *A&A*, 408, 193
- Krüger, D. & Sedlmayr, E. 1997, *A&A*, 321, 557
- Kurucz, R. & Bell, B. 1995, Atomic spectral line database from CD-ROM 23 of R. L. Kurucz, <https://web.cfa.harvard.edu/amp/ampdata/kurucz23/sekur.html>
- Li, G., Gordon, I. E., Le Roy, R. J., et al. 2013, *J. Quant. Spectr. Rad. Transf.*, 121, 78
- Li, G., Gordon, I. E., Rothman, L. S., et al. 2015, *ApJS*, 216, 15
- Lide, R. 1995, *CRC Handbook of Chemistry and Physics*, 78th edn. (CRC Press, Boca Raton, FL.)
- Liu, J., Jiang, B. W., Li, A., & Gao, J. 2017, *MNRAS*, 466, 1963
- Low, F. J. 1970, *Nature*, 227, 1333
- Marigo, P., Aringer, B., Girardi, L., & Bressan, A. 2022, *ApJ*, 940, 129
- Marini, E., Dell’Agli, F., Kamath, D., et al. 2023, *A&A*, 670, A97
- Masseron, T., Plez, B., Van Eck, S., et al. 2014, *A&A*, 571, A47
- Mattsson, L., De Cia, A., Andersen, A. C., & Petitjean, P. 2019, *A&A*, 624, A103
- Mattsson, L. & Sandin, C. 2021, *Universe*, 7, 113 (MS21)
- Mattsson, L., Wahlin, R., & Höfner, S. 2010, *A&A*, 509, A14
- Mattsson, L., Wahlin, R., Höfner, S., & Eriksson, K. 2008, *A&A*, 484, L5
- McKemmish, L. K., Masseron, T., Hoeijmakers, H. J., et al. 2019, *MNRAS*, 488, 2836
- McKemmish, L. K., Syme, A.-M., Borsosvzky, J., et al. 2020, *MNRAS*, 497, 1081
- McKemmish, L. K., Yurchenko, S. N., & Tennyson, J. 2016, *MNRAS*, 463, 771
- Molster, F. J., Waters, L. B. F. M., & Kemper, F. 2010, in *Lecture Notes in Physics*, Berlin Springer Verlag, ed. T. Henning, Vol. 815, 143–201
- Molster, F. J., Waters, L. B. F. M., & Tielens, A. G. G. M. 2002, *A&A*, 382, 222
- Olofsson, H., González Delgado, D., Kerschbaum, F., & Schöier, F. L. 2002, *A&A*, 391, 1053
- Owens, A., Dooley, S., McLaughlin, L., et al. 2022, *MNRAS*, 511, 5448
- Paulose, G., Barton, E. J., Yurchenko, S. N., & Tennyson, J. 2015, *MNRAS*, 454, 1931
- Polyansky, O. L., Kyuberis, A. A., Zobov, N. F., et al. 2018, *MNRAS*, 480, 2597
- Roueff, E., Abgrall, H., Czachorowski, P., et al. 2019, *A&A*, 630, A58
- Rybicki, G. & Lightman, A. 1979, *Radiative Processes in Astrophysics* (WILEY-VCH Verlag, Weinheim)
- Sandin, C. & Höfner, S. 2003, *A&A*, 398, 253
- Sandin, C. & Höfner, S. 2004, *A&A*, 413, 789 (Paper III)
- Sandin, C. & Mattsson, L. 2020, *MNRAS*, 499, 1531 (Paper V)
- Sharp, C. M. & Huebner, W. F. 1990, *The Astrophysical Journal Supplement Series*, 72, 417
- Shemansky, D. E. 1969, *J. Chem. Phys.*, 51, 689
- Smirnov, A. N., Solomonik, V. G., Yurchenko, S. N., & Tennyson, J. 2019, *Physical Chemistry Chemical Physics (Incorporating Faraday Transactions)*, 21, 22794
- Somogyi, W., Yurchenko, S. N., & Yachmenev, A. 2021, *J. Chem. Phys.*, 155, 214303
- Sorensen, J. J. & Bernath, P. F. 2021, *ApJ*, 923, 234
- Späth, H. 1995, *Two Dimensional Spline Interpolation Algorithms* (A K Peters/CRC Press, New York)
- Syme, A.-M. & McKemmish, L. K. 2020, *MNRAS*, 499, 25
- Syme, A.-M. & McKemmish, L. K. 2021, *MNRAS*, 505, 4383
- Tennyson, J., Yurchenko, S. N., Al-Refaie, A. F., et al. 2020, *J. Quant. Spectr. Rad. Transf.*, 255, 107228
- Tosi, S., Dell’Agli, F., Huerta-Martinez, E., & Ventura, P. 2022, *Universe*, 8, 270
- Underwood, D. S., Tennyson, J., Yurchenko, S. N., et al. 2016, *MNRAS*, 459, 3890
- Upadhyay, A., Conway, E. K., Tennyson, J., & Yurchenko, S. N. 2018, *MNRAS*, 477, 1520
- Utenthaler, S., McDonald, I., Bernhard, K., Cristallo, S., & Gobrecht, D. 2019, *A&A*, 622, A120
- Verner, D. A., Ferland, G. J., Korista, K. T., & Yakovlev, D. G. 1996, *ApJ*, 465, 487
- Verner, D. A. & Yakovlev, D. G. 1995, *A&AS*, 109, 125
- Western, C. M. 2017, *J. Quant. Spectr. Rad. Transf.*, 186, 221
- Western, C. M., Carter-Blatchford, L., Crozet, P., et al. 2018, *J. Quant. Spectr. Rad. Transf.*, 219, 127
- Whitelock, P. A., Menzies, J. W., Feast, M. W., et al. 2009, *MNRAS*, 394, 795
- Wickramasinghe, N. C. 1972, *MNRAS*, 159, 269
- Woolf, N. J. & Ney, E. P. 1969, *ApJ*, 155, L181
- Yousefi, M., Bernath, P. F., Hodges, J., & Masseron, T. 2018, *J. Quant. Spectr. Rad. Transf.*, 217, 416
- Yurchenko, S. N., Al-Refaie, A. F., & Tennyson, J. 2018a, *A&A*, 614, A131
- Yurchenko, S. N., Amundsen, D. S., Tennyson, J., & Waldmann, I. P. 2017, *A&A*, 605, A95
- Yurchenko, S. N., Mellor, T. M., Freedman, R. S., & Tennyson, J. 2020, *MNRAS*, 496, 5282
- Yurchenko, S. N., Szabó, I., Pyatenko, E., & Tennyson, J. 2018b, *MNRAS*, 480, 3397
- Yurchenko, S. N. & Tennyson, J. 2014, *MNRAS*, 440, 1649
- Yurchenko, S. N., Tennyson, J., Syme, A.-M., et al. 2022, *MNRAS*, 510, 903

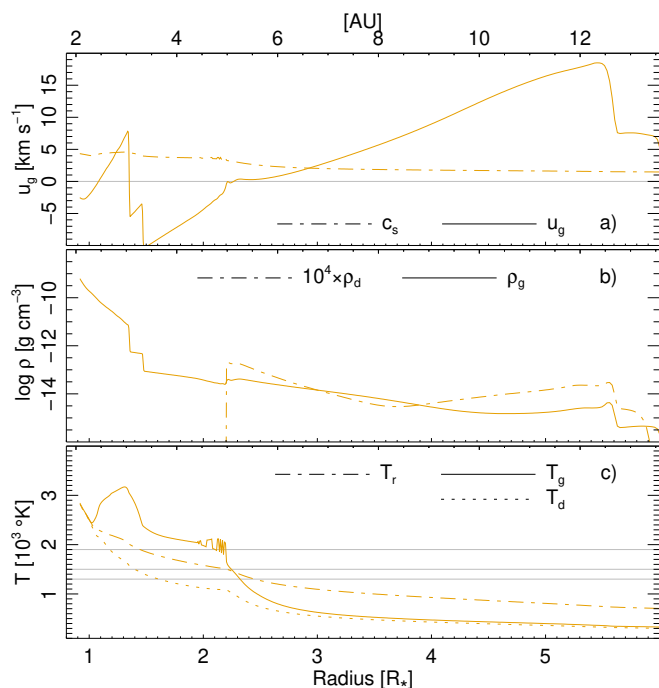


Fig. B.1. Radial structure of a snapshot of setup L3.85T24 for the inner modelled region. A PC model using the gas opacities of Aringer is shown with orange lines. The 3 panels show: (a) gas velocity u_g , sound speed c_s ; (b) gas density ρ_g , dust density $10^4 \times \rho_d$ (log); and (c) gas temperature T_g , radiative temperature T_r , and dust temperature T_d . All properties are drawn versus the stellar radius R_* (lower axis) and astronomical units (AU; upper axis). Grey horizontal lines are guides.

Appendix A: Calculation of κ_{bf} and κ_{ff}

Here is a brief description of the methods and data used in the determination of the bound-free and free-free opacities, which are calculated using the JEKYLL code (Ergon et al. 2018; Ergon & Fransson 2022). As in the calculations of our bound-bound opacities, we first determine cross sections of bound-free level populations and then calculate opacities based on the physical conditions.

The photo-ionization cross-sections for ground states are calculated using analytic fits of Verner & Yakovlev (1995) and Verner et al. (1996), and for the lowest excited states of He I, C I, O I, Mg I, Mg II, Si I, S I, and Ca II, using data from TOPBASE of the Opacity Project⁸. For all other excited states, photo-ionization cross-sections are calculated using a hydrogenic approximation by Rybicki & Lightman (1979). Bound-free opacities are then calculated based on LTE populations of excited and ionized states for given values of density, temperature, and composition. Atomic data (excitation and ionization energies and statistical weights) are obtained from the Atomic Spectra Database of NIST⁹ and the online tables by R. Kurucz¹⁰.

Free-free opacities $\kappa_{ff,i}$ are calculated for each ion i separately using an expression that depends on the same electron and ion densities that are used to calculate bound-free opacities (e.g. Eq. (5.149) in Hubeny & Mihalas 2015).

Appendix B: On the role of the gas opacity data

Developing our new oxygen-rich chemistry models, we calculated test wind models using the same gas opacity table that B19 use (the data are described by Aringer 2000; Aringer et al. 2009). The first test models indicated a problem when starting the stellar wind; some kind of noise appears in the gas temperature of all models when dust is present and where $T_g \approx 2000$ K. We show an example of such noise in Fig. B.1, which presents a snapshot of a stellar wind model where calculations have just begun. The noise occurs in the temperature in the interval $1.9 \lesssim r \lesssim 2.2 R_*$. The same noise is [spatially] unresolved in models using $N_d = 100$ grid points (not shown), and here, the problem is much smaller. The problem becomes prohibitive in drift models, which are more sensitive to variations of this kind. The origin of the noise is unknown, but no terms in the radiation hydrodynamic equations appear to be responsible considering the noise always appears at the same gas temperature. Therefore, we hypothesized that the noise originates in the gas opacity data.

We calculated new gas opacity tables based on ExoMOL data, see Sect. 4.2.1. The extant and new opacity data sets are compared in Fig. B.2, for the wavelength $\lambda = 1 \mu\text{m}$. The figures show a somewhat similar pattern. Discrepancies are smaller at the lowest temperatures, where the offset is about 0.7 dex (not shown). Differences are also larger at lower densities. At higher temperatures and lower densities, our new bound-bound opacities drop faster to low values. The region of typically assumed densities and temperatures is indicated in the figure. Here, bound-bound opacities of molecules dominate and our values are about one dex lower than those of Aringer et al.. The same low values are not seen in the opacity data of Aringer et al., whose opacity values at the higher temperatures $T \gtrsim 4000$ K are up to 10^6 times higher than our values. More recent publicly available weighted grey opacities (ÆSOPUS project of Marigo et al. 2022) that were at some point based on the opacity data we already have include opacities of both atoms and ions at higher temperatures (Aringer, priv. comm.). In our new opacities, data at such higher temperatures only consist of free-free and bound-free components. The opacity data of Aringer et al. show values that appear to be more constant at higher temperatures and lower densities; their data show less structure than our new opacities.

With our new opacities, the stellar wind calculations are not hampered by the same kind of noise at $T \approx 2000$ K described above. The extant opacity tables only allow us to speculate on why these data give rise to noise in the temperature when we use them to attempt to calculate a stellar wind.

⁸ <https://cdsweb.unistra.fr/topbase/topbase.html>

⁹ <https://www.nist.gov/pml/atomic-spectra-database>

¹⁰ <https://web.cfa.harvard.edu/amp/ampdata/kurucz23/sekur.html>

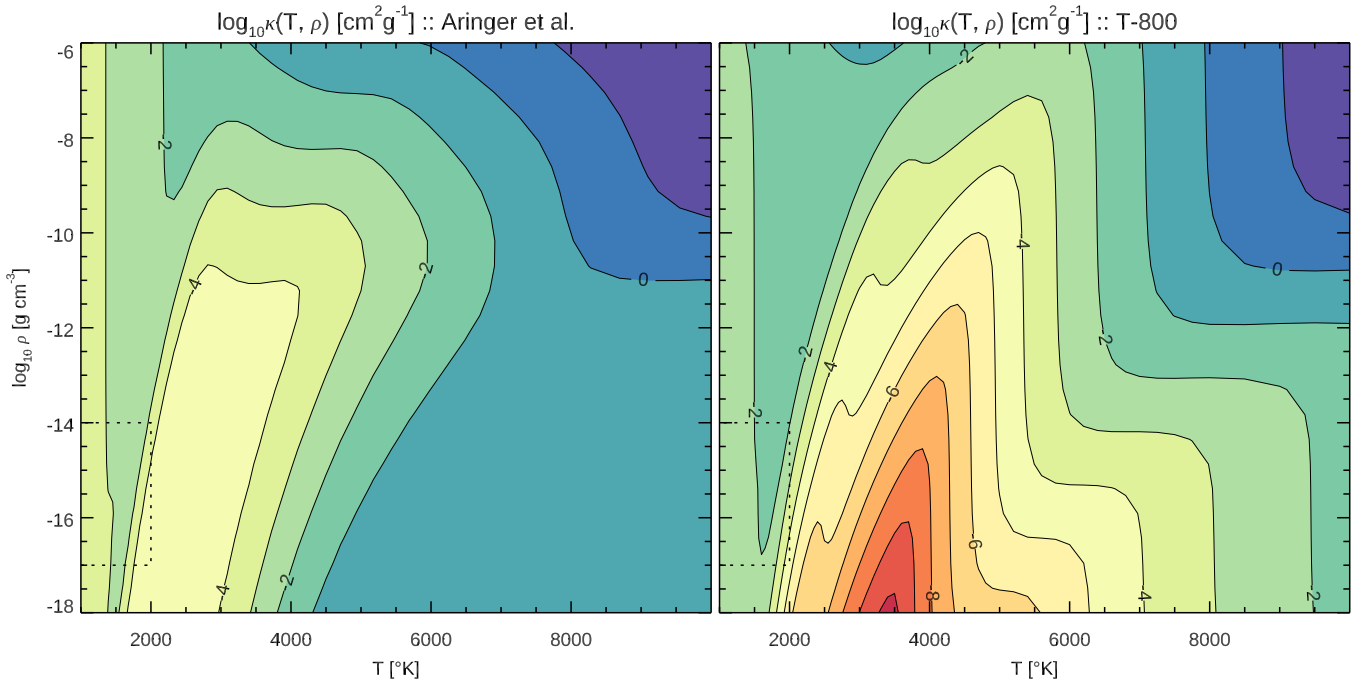


Fig. B.2. The total gas opacity at the wavelength that is the closest to $\lambda = 1 \mu\text{m}$ for the data of Aringer et al. (left panel) and our new data (right panel). The opacity is shown colour coded versus the temperature (x -axis) and the gas density (y -axis). All integers on the contour lines are negative (but 0). The temperature and density ranges are $1000 \leq T \leq 10\,000 \text{ K}$ and $-18 \leq \log \rho \leq -6 \text{ g cm}^{-3}$, respectively. The two panels use the same ranges and colour palette. The dotted box delimits densities and temperatures in the wind formation region of the model shown in Fig. 4.